Journal of
Materials Chemistry C

Accepted Manuscript

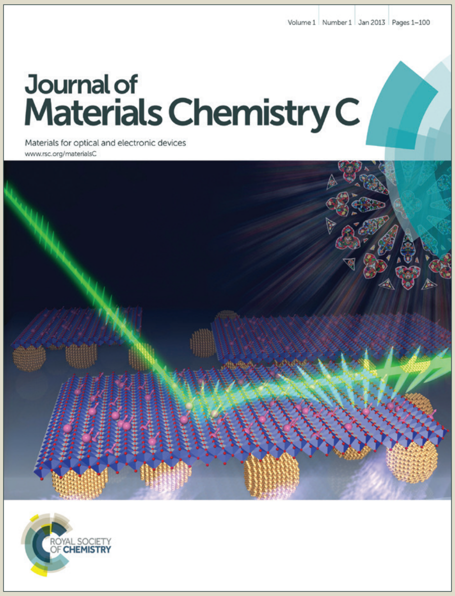

ROYAL SOCIETY
OF **CHEMISTRY**

www.rsc.org/materialsC

Journal Name RSCPublishing

ARTICLE

# $p$-($p$,$\pi$*) interaction mechanism revealing and accordingly designed new member in deep-ultraviolet NLO borates $Li_nM_{n-1}B_{2n-1}O_{4n-2}$ (M=Cs/Rb, n=3, 4, 6)

Bingbing Zhang,[a,b] Zhihua Yang,[*,a] Yun Yang,[*,a] Ming-Hsien Lee,[c] Shilie Pan,[*,a] Qun Jing,[a,b] and Xin Su[a,b]

Received 00th January 2012,
Accepted 00th January 2012

DOI: 10.1039/x0xx00000x

www.rsc.org/

The exploration on the compounds in the complex alkali metal borate system had resulted in the discovery of a class of deep-ultraviolet second-order nonlinear optical (NLO) materials, $Li_3Cs_2B_5O_{10}$ (L3CBO), $Li_4Cs_3B_7O_{14}$ (L4CBO), and $Li_6Rb_5B_{11}O_{22}$ (L6RBO), which can be reduced to a general formula of $Li_nM_{n-1}B_{2n-1}O_{4n-2}$ (M=Cs/Rb, n=3, 4, 6). All of the three crystals exhibit a short UV cutoff edge (below 190 nm), and share a class of topologically similar BO groups interconnected by $LiO_n$ (n= 4, 5), Rb/$CsO_n$ (n=8, 9, 10). The mechanism of NLO properties of this class of crystals were studied using band-resolved and SHG-density methods based on the first-principles theory. The results reveal that the "charge-transfer excitation" from the non-bonding 2*p* occupied states of O atoms to the $\pi$* and 2*p* unoccupied states of $BO_3$ substructure in BO groups is the key mechanism of NLO properties of this material family. Through systematic analyses on the relationship between crystal structure and NLO effects, a new crystal, $Li_4Rb_3B_7O_{14}$ was designed and subsequently synthesized through solid state reaction, which is isomorphic with $Li_4Cs_3B_7O_{14}$, exhibit a short UV cutoff edge (below 190 nm) and a SHG response of 2/3 × KDP.

## Introduction

The increase demand of nonlinear optical (NLO) crystals,[1-6] especially those outputting deep-UV/UV coherent light, has prompted intensive effort in search for new NLO crystals. Borate crystals, as NLO materials, have attracted much attention for their characteristics such as being transparent in the wide range of wavelengths, having high damage threshold. Therefore, many borates have been widely used in deep-UV/UV and visible regions, such as $\beta$-$BaB_2O_4$ (BBO),[7] $LiB_3O_5$ (LBO),[8] $CsB_3O_5$ (CBO),[9] $CsLiB_6O_{10}$ (CLBO),[10] $KBe_2BO_3F_2$ (KBBF).[11] Among these borates, more than half of them are alkali metal borates (LBO, CBO, and CLBO), which have become major NLO crystals owing to their appropriate efficient SHG coefficients and superiority in transmission of UV waveband. Especially for CLBO, it is one of the most important crystals for 266 nm coherent radiation.[12] In these alkali metal borates, the BO groups play an important role to implement frequency doubling,[13] and the alkali metal cations are beneficial for UV transmission without *d-d* electron transitions. These are two basic criteria for a good deep-UV/UV NLO material. Therefore, alkali metal borates are a promising system to look for new NLO crystals and worth further research.

A full understanding of the mechanism of NLO effects in crystals can help us design and search new excellent NLO crystals more efficiently. During past decades, lots of efforts have been made to explore the inner relations between the composition/microscopic structures and macroscopic NLO properties of crystals. The "anionic group theory",[14] proposed by Chen et al., has proven to be successful in searching new borate NLO crystals.[15] With the rapid development of scientific computational resources, getting an in-depth description of structure, electronic structure, and optical properties are practicable based on the first-principles method. On the bases of the electronic structure, the NLO property can be calculated and analyzed. Furthermore, the orbitals and atoms/atom groups giving major contribution to SHG coefficient can be highlighted by the band-resolved method[16] and SHG density method[17]. This would be very useful to deeply understand the inner mechanism of NLO effects and to guide the design of new NLO materials. For alkali metal borate system, the design strategy is described as follow. i) Find out the NLO-active units in crystal structure. ii) Clarify the influence of the arrangement of these NLO-active units on the macroscopic NLO response. iii) Design new crystals by increasing the density and SHG strength of NLO-active units and optimizing the arrangement of them.

Recently, a class of alkali metal borates, $Li_3Cs_2B_5O_{10}$ (L3CBO), $Li_4Cs_3B_7O_{14}$ (L4CBO), and $Li_6Rb_5B_{11}O_{22}$ (L6RBO) had been synthesized using the conventional solid stated reaction method by our group.[18-20] All of these complex alkali metal borate series exhibit short wavelength UV cutoff edges (<190 nm) and display a measurable NLO effects. Not only their chemical formulas have certain regularity and can be reduced to a general formula of $Li_nM_{n-1}B_{2n-1}O_{4n-2}$ (M=Cs/Rb, n=3, 4, 6), but some interesting regularities exist in their structures. All the three crystals have the same fundamental building blocks (FBB). They were built from isolated BO groups interconnected by $LiO_n$ (n= 4, 5), Rb/$CsO_n$ (n=8, 9, 10). It is worth mentioning that BO groups have the same topological structure. These material series provide the valuable research matter for the inner relations between the composition/microscopic structures and macroscopic NLO properties of crystals.

In the paper, the electronic and NLO properties of these material series are studied using the first-principles method. We want to know the mechanisms of the SHG effects for the three compounds: (1) Where does the SHG effect originate from? That is, find out the NLO-active units in crystal structure. (2) How do the arrangements of the NLO-active units affect macroscopic NLO effects? To clarify these questions, the following contents were considered. The electronic structure and NLO properties were calculated. The band-resolved method and SHG-density method were used to find out NLO-active electronic states and corresponding structural units. The topological properties of BO groups were analyzed systematically. The relationships among topological geometry structure, microscopic electronic structure and macroscopic NLO properties were discussed. According to the in-depth understanding of the mechanisms of the NLO property in these crystal series, we predict and synthesize a new crystal, $Li_4Rb_3B_7O_{14}$ (L4RBO), which is a new member of these series of crystals and is isomorphic with L4CBO, just as we expected, which have a larger NLO response than L4CBO.

## Computational Details and Methods

### Electronic Structures and Linear Optical Properties

The electronic structures and optical property calculations of the title compounds were performed by employing CASTEP[21], a plane-wave pseudopotential package. Norm-conserving pseudopotentials (NCP) [22, 23, 24] were used, and the valence electrons were set as $2s^1$ configuration for lithium, $2s^22p^1$ for boron, $2s^22p^4$ for oxygen, $5s^25p^66s^1$ for caesium and $4s^24p^65s^1$ for rubidium, respectively. The exchange-correlation functional was Perdew-Burke-Emzerhoff (PBE) functional within the generalized gradient approximation (GGA). [25] The plane-wave energy cutoff was set at 830.0 eV. The k-point separation for each material was set less than 0.035 Å$^{-1}$ in the Brillouin zone, resulting in corresponding Monkhorst-Pack k-point meshes 6×6×3, 7×7×2, and 5×5×3, respectively. Self-consistent field (SCF) calculations were performed with a convergence criterion of $1\times10^{-6}$ eV/atom on the total energy. For comparison, the local-density approximation (LDA) for the exchange-correlation energy was also used. Same accuracy level of parameter setting was adapted in GGA and LDA calculations.

### SHG Coefficients

The SHG coefficients were calculated from the band wave functions by using the so-called length-gauge formalism derived by Aversa and Sipe[26] at a zero frequency limit. The static second-order susceptibilities $\chi_{\alpha\beta\gamma}^{(2)}$ can be written as, [27]

$$\chi_{\alpha\beta\gamma}{}^{(2)}=\chi_{\alpha\beta\gamma}{}^{(2)}(\mathrm{VE})+\chi_{\alpha\beta\gamma}{}^{(2)}(\mathrm{VH})+\chi_{\alpha\beta\gamma}{}^{(2)}(\mathrm{two\text{-}bands})\ . \quad (1)$$

In this sum-over-states type formalism, the total SHG coefficient $\chi^{(2)}$ are divided into contribution from Virtual-Hole (VH), Virtual-Electron (VE) and Two-Band (TB) processes. The contribution from TB process is so small that can be neglected. The formulas for calculating $\chi_{\alpha\beta\gamma}{}^{(2)}$(VE), $\chi_{\alpha\beta\gamma}{}^{(2)}$(VH), and $\chi_{\alpha\beta\gamma}{}^{(2)}$(two bands) are as follows,

$$\chi_{\alpha\beta\gamma}{}^{(2)}(VE)=\frac{e^3}{2\hbar}\sum\int\frac{d^3k}{4\pi^3}P(\alpha\beta\gamma)\,\mathrm{Im}\left[P_{vv'}^{\alpha}P_{cv'}^{\beta}P_{cv}^{\gamma}\right]\left(\frac{1}{\omega_{cv}^3\omega_{v'c}^2}+\frac{2}{\omega_{vc}^4\omega_{cv'}}\right)\ ,\quad (2)$$

$$\chi_{\alpha\beta\gamma}{}^{(2)}(VH)=\frac{e^3}{2\hbar}\sum\int\frac{d^3k}{4\pi^3}P(\alpha\beta\gamma)\,\mathrm{Im}\left[P_{cv}^{\alpha}P_{cc'}^{\beta}P_{c'v}^{\gamma}\right]\left(\frac{1}{\omega_{cv}^3\omega_{vc'}^2}+\frac{2}{\omega_{vc}^4\omega_{c'v}}\right)\ ,\quad (3)$$

$$\chi_{\alpha\beta\gamma}{}^{(2)}(two-bands)=\frac{e^3}{2\hbar}\sum\int\frac{d^3k}{4\pi^3}P(\alpha\beta\gamma)\frac{\mathrm{Im}\left[P_{vc}^{\alpha}P_{cv}^{\beta}(P_{vv}^{\gamma}-P_{cc}^{\gamma})\right]}{\omega_{vc}^5}\ .\quad (4)$$

Here, $\alpha$, $\beta$, $\gamma$ are Cartesian components, v and v′ denote valence bands, c and c′ refer to conduction bands, and P($\alpha\beta\gamma$) denotes full permutation. The band energy difference and momentum matrix elements are denoted as $\hbar\omega_{ij}$ and $P_{ij}{}^{\alpha}$, respectively.

### Band-resolved Method and SHG-density Method

In order to investigate the respective contribution of individual electronic states to SHG coefficients, the band-resolved method for analyzing $\chi^{(2)}$ within energy band framework was adopted in this work. This analysis scheme proposed partially summing over two out of the three band indices for $\chi_{\alpha\beta\gamma}{}^{(2)}$(VE) or $\chi_{\alpha\beta\gamma}{}^{(2)}$(VH) in Eqs.(2-3). Two kinds of summing sequences induce a consequent decomposition of the SHG strength into occupied and unoccupied band representations of orbital contributions. The band-resolved SHG coefficient can thus be visualized in an energy level-by-level basis, which explicitly exhibits the orbital contribution to total $\chi^{(2)}$. By using this method, the dominant states giving major contributions to a SHG process can be identified and further analyzed.

To clarify the mechanism of the SHG response further for the complicated structures we studied, another powerful method called SHG-density was employed in our work to visualize the part of their electronic structure subsystem which causes SHG. The SHG-density method was performed by using the effective SHG of each band (occupied or unoccupied) as weighting coefficient (after normalized with total VE or VH $\chi^{(2)}$ value) to sum the probability densities of all occupied or unoccupied states. Therefore, this method ensures quantum states which cause SHG can be shown together as these occupied or unoccupied "SHG-densities", while states irrelevant to SHG will not be shown. The origin of SHG optical nonlinearity can therefore be highlighted in the real space through the resulting distribution of such densities.

## Experimental Section

### Crystal Growth

Single crystals of $Li_4Rb_3B_7O_{14}$ were grown by melting a mixture of $Li_2CO_3$ (98.0%, Tianjin Yaohua Chemical Reagent Co., Ltd), $Rb_2CO_3$ (99.5%, Institute of Xinjiang metal), and $H_3BO_3$ (99.5%, Tianjin Baishi Chemical Co., Ltd) at a molar ratio of 6:5:22 in a platinum crucible that was placed into a vertical, programmable temperature furnace. It was heated to 750 °C, held at this temperature for 24 h to insure the solution melts completely and homogeneously, and then quickly cooled to the initial crystallization temperature, 570 °C, held at this temperature for 2 h, then slowly cooled to 520 °C at a rate of 5 °C/h, and subsequently cooled to 420 °C at a cooling rate of 10 °C/h, finally cooled to 100 °C at a cooling rate of 20 °C/h. Colorless block crystals were separated from the crucible for structural characterization. Crystals suitable for X-ray diffraction were selected under an optical microscope.

### Solid-State Synthesis

Polycrystalline samples of L4RBO were synthesized via solid-state reactions from mixtures of $Li_2CO_3$, $Rb_2CO_3$, and $H_3BO_3$ as the starting components in a molar ratio of 4:3:14. The sample was heated to 550 °C slowly and held at this temperature for 48 h with several intermediate grindings and mixings.

The purity of the sample was checked by XRD diffraction. The XRD measurements on L4RBO were performed at room temperature on a Bruker D2 advanced diffractometer equipped with a diffracted-beamed monochromator set for Cu K$\alpha$ (k=1.5418 Å) radiation. The diffraction patterns were taken from 10° to 70° ($2\theta$). The measured powder XRD pattern matches the one simulated from single-crystal XRD studies.

### Structure Determination

The crystal structure of L4RBO was investigated by single-crystal XRD on a Bruker SMART APEX II CCD diffractometer using monochromatic Mo K$\alpha$ radiation ($\lambda$= 0.71073 Å) at 153(2) K and integrated with the SAINT program.[28] All calculations were performed with programs from the SHELXTL crystallographic software package. The structure was solved by direct methods using SHELXS-97.[29] Final least-squares refinement is on $F_o^2$ with data having $F_o^2 \geqslant 2\sigma (F_o^2)$. The space group symmetry was verified using the ADDSYM algorithm from the program PLATON[30] and no higher symmetries were found. The final refined atomic positions and isotropic thermal parameters are given in Table S1 in the ESI†. The main interatomic distances and angles are listed in Table S2.

### Vibrational Spectroscopy

IR spectroscopy was carried out with the objective of specifying and comparing the coordination of boron in L4RBO. The mid-IR spectrum was obtained at room temperature via a Shimadzu IRAffinity-1 Fourier transform IR spectrometer in the 400-4000 cm$^{-1}$ range. The sample was mixed thoroughly with dried KBr (5 mg of the sample and 500 mg of KBr).

### Thermal Analysis

Thermal gravimetric analysis (TGA) and differential scanning calorimetry (DSC) were carried out on NETZSCH STA 449C instrument at a temperature range of 30-800 °C with a heating rate of 10 °C /min in an atmosphere of flowing $N_2$.

### UV-Vis-NIR Diffuse Reflectance Spectroscopy

UV-Vis-NIR diffuse reflectance of L3CBO, L4CBO, L4RBO and L6RBO crystalline samples was collected at room temperature with a SolidSpec-3700DUV spectrophotometer using fluororesin as a standard in the wavelength range from 190 to 2600 nm. and reflectance spectra were converted to absorbance by the Kubelka-Munk transformation.[31, 32]

### NLO Measurements

Powder second-harmonic generation (SHG) tests were carried out on L4RBO by the Kurtz-Perry method using a pulsed Nd:YAG laser with a wavelength of 1064 nm. A detailed description of the equipment and the methodology used has been published.[33] Since SHG efficiencies are known to depend strongly on particle size, polycrystalline samples were ground and sieved into the following particle size ranges: 38−55, 55−88, 88−105, 105−150, and 150−200 $\mu$m. Microcrystalline KDP were also ground and sieved into the same particle size ranges and served as a reference. Powders with particle sizes of 105−150μm were used for comparing SHG intensities.

## Results and Discussion

### Isolated $[B_{2n-1}O_{4n-2}]$ Topological Structure

L3CBO crystallizes in the space group $C222_1$, and cell dimensions are $a$ = 7.2256(2) Å, $b$ = 11.6583(4) Å, and $c$ = 12.8717(4) Å. It exhibits an infinite three-dimensional (3D) network composed of isolated $B_5O_{10}$ groups interconnected by Li and Cs atoms (Figure 1a). L4CBO belongs to the trigonal system and the space group $P3_121$ with lattice parameters $a = b$ = 6.9313(6) Å, $c$ = 26.799(3) Å. Isolated $B_7O_{14}$ groups, Li and Cs atoms together form the infinite 3D network of L4CBO (Figure 1b). L6RBO is composed of Li, Rb atoms and isolated $B_{11}O_{22}$ groups, which also expands a 3D network with the monoclinic space group $C2$, and unit cell parameters are $a$ = 11.6256(5) Å, $b$ = 7.1010(3) Å, $c$ = 13.7442(5) Å, $\beta$ = 106.871(3)° (Figure 1c).

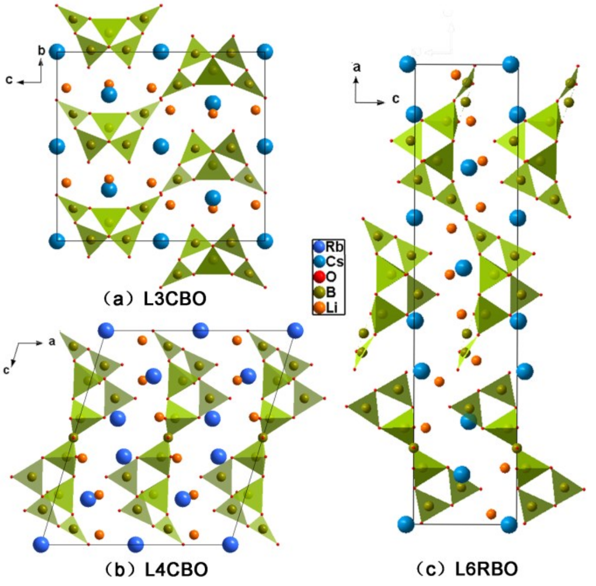

**Figure 1.** The crystal structures of L3CBO, L4CBO, and L6RBO and arrangement of the BO groups in corresponding crystals.

In LMBO (abbreviation for $Li_nM_{n-1}B_{2n-1}O_{4n-2}$(M=Cs/Rb, n=3, 4, 6)) series, the BO groups are topologically similar.[34] From Figure 2, one can see the '8'-shaped BO ring ($B_5O_{10}$) in L3CBO composed of two $B_3O_7$ (2△+□, △ and □ represent $BO_3$ and $BO_4$ groups, respectively) by sharing a four-fold coordinated B atom. And in L4CBO, a terminal $BO_3$ (△) in the '8'-shaped BO ring is replaced by a $BO_4$ connecting other two $BO_3$ to form a double-'8'-shaped-ring ($B_7O_{14}$). Similarly, the $B_7O_{14}$ extends to $B_{11}O_{22}$, composed of three $B_3O_8$ rings being between two $B_3O_7$, which becomes FBB of L6RBO. Following the evolutionary procedure of the existing topological structure of $B_{2n-1}O_{4n-2}$ (n=3, 4, 6), the intermediate structure $B_9O_{18}$, between $B_7O_{14}$ and $B_{11}O_{22}$, is also a member (n=5) (see Figure 2).

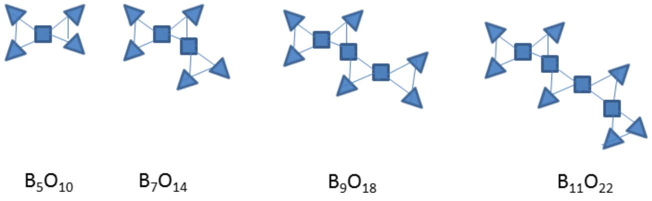

**Figure 2.** The isolated BO topological structures, $B_5O_{10}$, $B_7O_{14}$, and $B_{11}O_{22}$ exist in L3CBO, L4CBO, and L6RBO, respectively. $B_9O_{18}$ is an intermediate structure between $B_7O_{14}$ and $B_{11}O_{22}$.

## Electronic Structure

The band structures of LMBO series calculated along selected high symmetry k-points within GGA are shown in Figure S1 in the ESI†. Although the four crystals considered here have different symmetries, their band structures are qualitatively similar to one another. They are all indirect gap materials with calculated band gaps being 4.59, 4.62, and 4.37 eV, which are relatively smaller than experimental optical gaps obtained by the extrapolation method,[35] 6.30, 6.01, and 5.28 eV (see Figure S2) due to a typical disadvantage in density functional theory (DFT) calculations. These differences will be corrected using a so-called scissors energy shift when evaluating optical properties based on DFT band structure calculation results. There is no significant difference between the choices of commonly used exchange correlation functionals, as shown in Table 1.

| | Experimental | Calculated | |
|---|---|---|---|
| | | GGA | LDA |
| L3CBO | 6.30 | 4.59 | 4.29 |
| L4CBO | 6.01 | 4.62 | 4.32 |
| L4RBO | 5.51 | 4.27 | 3.98 |
| L6RBO | 5.28 | 4.37 | 4.08 |

**Table 1.** Comparison of the experimental and calculated energy band gaps by GGA and LDA functionals for the LMBO series (Unit: eV).

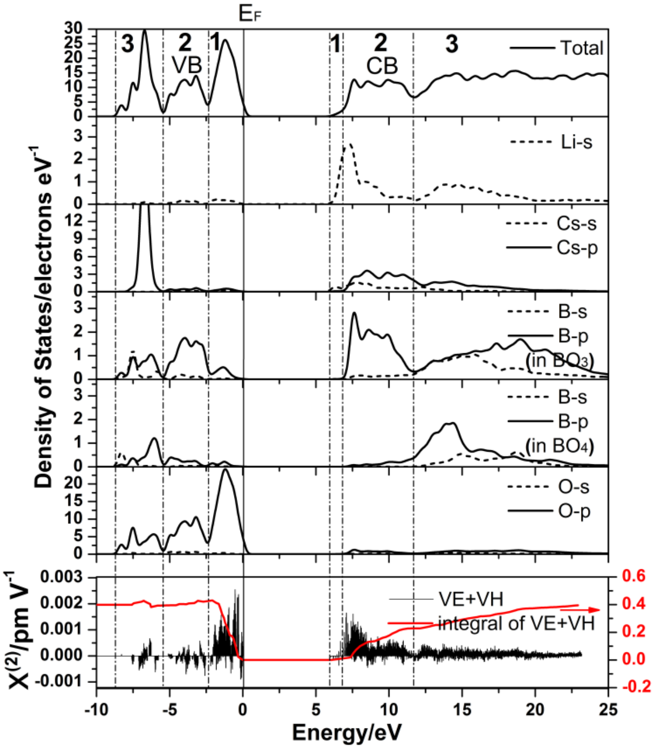

**Figure 3.** The comparison between the PDOS (top) and band-resolved $\chi^{(2)}$ (bottom) of L4CBO. The band-resolved $\chi^{(2)}$ and their integral values (red line) illustrate that the states at VB-1 CB-2, and CB-3 make the significant contributions to the SHG coefficient.

The partial density of state (PDOS) is one useful method to analyze the composition and origin of the calculated bands. The PDOS diagrams of LMBO series are shown in Figure 3 (L4CBO) and Figure S3 (L3CBO and L6RBO) with assigned numbers to mark different regions in the valence bands (VB) and conduction bands (CB) for the convenience of discussion. Like the band structures, their PDOSs are also similar to one another due to all the three crystals having the similar FBB. As an example, Figure 3 shows the PDOS of Li atoms, Cs atoms, three- and four-fold coordination B atoms, and O atoms in L4CBO, respectively. Referring to the orbital calculation and X-ray photoemission spectroscopy (XPS) of $[B_3O_7]^{5-}$ group in LBO,[36] the marked regions characterized by different bonding types. Some representative orbital shapes in these six regions are also drawn (see Figure S4) that exactly confirm the orbital calculation results of $[B_3O_7]^{5-}$ group in LBO. Below Fermi level ($E_F$), the region VB-3 is mainly occupied by 2*p* states of B and O as well as B-O $\sigma$-bonding states (Figure S4a). VB-2 is mainly occupied by 2*p* states of three-fold B and O atoms and B-O $\pi$-bonding states (Figure S4b). VB-1 is mainly occupied by the O non-bonding 2*p* states (Figure S4c). Above $E_F$, CB-1 is only occupied by Li 2*s* and Cs 6*s* states. The 2*p* states of three-fold B and O atoms as well as formed B-O $\pi$-antibonding ($\pi$*) states are located at CB-2 region (Figure S4e). The 2*p* states of four-fold B and O atoms, $\sigma$-antibonding ($\sigma$*) are located at CB-3 region (Figures S4f).

**Mechanism of NLO Properties**

The calculated SHG coefficients of the LMBO series are listed in Table 2 compared with experimental values (The calculation method is described in the last section). The experimental SHG intensities were obtained by powder SHG tests,[18-20] and compared with that of KDP crystal ($|d_{eff}^{SHG}(1064nm)| \approx 0.38$ pm/V). They are well in agreement with the experimental values of L4CBO, and L6RBO, while that of L3CBO is relatively smaller than the experimental result. Considering the reliability of the length-gauge formalism that successfully predict the SHG coefficients of a large number of crystals, for example, BBO,[37] LBO,[13] CBO,[13] CLBO,[13] KBBF,[38] $BiB_3O_6$ (BIBO),[39] $Sr_2Be_2B_2O_7$ (SBBO) family,[40] the SHG intensities of L3CBO was remeasured. The polycrystalline samples were prepared by grinding a high quality single crysltal and sieved into particle size ranges of 150−200 μm. The result is about 1/5 KDP which is really smaller than previous measurement and in agreement with our calculation. It proves that our calculation method has reasonably high reliability and usefulness for predicting SHG coefficients.

| Crystal | Exp. | Cal. $d_{ij}$ ( pm/V) | | VE | VH |
|---|---|---|---|---|---|
| L3CBO | ≈1/2KDP[19] | $d_{14}$ | −0.019 | −0.063 | 0.044 |
| L4CBO | ≈1/2KDP[20] | $d_{11}$ | 0.259 | 0.194 | 0.065 |
| L4RBO | ≈2/3KDP | $d_{11}$ | 0.335 | 0.309 | 0.026 |
| L6RBO | ≈2/3KDP[12] | $d_{14}$ | −0.064 | −0.054 | −0.017 |
| | | $d_{16}$ | −0.229 | −0.236 | 0.007 |
| | | $d_{22}$ | 0.238 | 0.219 | 0.019 |
| | | $d_{23}$ | −0.054 | −0.044 | −0.010 |

**Table 2.** Comparisons of the calculated SHG coefficients with a correction of the band gap by using scissor operator and experimental powder SHG effect of the LMBO series.

Where does the SHG response of the title compounds originate from? To address that question in the energy representation, we investigate the respective contribution of each electron state to the SHG effect, and identify the specific states making the major contributions to SHG response using band-resolved method. The results are listed together with PDOS, and their integral contribution is also plotted. In L4CBO (Figure 3), for example, the occupied states that dominate the contribution to SHG concentrate in VB-1 region. This region is mainly occupied by O non-bonding 2*p* states and with B 2*p* states slightly mixed-in. In comparison, the unoccupied states that contribute to SHG concentrate in CB-2. In addition, CB-3 region also makes a contribution disperse in a wide range. The band-resolved result of L6RBO is similar to that of L4CBO. But, L3CBO exhibits a slightly different NLO behaviour from the above two crystals in the sense described below (Figure S3a). The states located at VB-1 region make a much smaller contribution to total $d_{14}$ SHG coefficient. This is due to the antiparallel of $B_5O_{10}$ groups in crystal (The proof will be provided in the analysis below). It is worth noting that the CB-1 region formed by Li *2s* and Cs *6s* (or Rb *5s*) states, has little contribution to SHG in the all three crystals despite these states occupy the bottom of CB.

To further identify the spatial distribution of the electronic states dominating SHG response, the SHG-density method was utilized in our work. The SHG-density can be divided into occupied and unoccupied states of Virtual-Electron (VE) and Virtual-Hole (VH), respectively. In this work, the VE process is analyzed because it dominates the SHG in the crystals studied (see Table 2). As clearly shown in Figure 4a for L4CBO, oxygen non-bonding 2*p* electrons are the dominant contributor to SHG coefficient in occupied states. It was also found that the off-ring O atoms play a much more important role to SHG effects than in-ring O atoms do in BO group. The PDOS of off-ring and in-ring O atoms (Figure S5) show that each off-ring O atoms have more non-bonding 2*p* states than that of the in-ring O atoms, and it is not surprising why off-ring O atoms make a bigger contribution. Similar conclusion was also found in BBO from the work of Duan et al.[41] The maximum SHG density around caesium atoms is only 3.5% of that of O atoms. Under this scale, lithium and boron atoms have no noticeable SHG density at all. Unlike occupied states where O *2p* non-bonding orbitals are the dominant contributor, in unoccupied states, two $BO_3$ substructures in $B_3O_7$ rings are the major source of SHG in L4CBO (Figure 4). The shape of SHG density around B and O atoms reveals an apparent contribution from the B-O $\pi$* and 2*p* states of B and O atoms in $BO_3$ substructure. What's even more remarkable is that $BO_3$ in $B_3O_8$ ring makes a much smaller influence than that of each $BO_3$ in $B_3O_7$ rings. It means that the combination of $BO_3$ in a BO hexatomic ring is more effective to SHG response than the summation of the two $BO_3$ in $B_3O_8$ ring. The same conclusion is also confirmed in L6RBO (see figure S6). There is little contribution coming from four-fold coordination B, and the maximum SHG density around it is 27.4% of that of $BO_3$ substructure. As for cations, caesium makes a little contribution similar to the four-fold coordination B. The contribution of lithium has not been found. The characteristic of SHG densities of L3CBO and L6RBO are similar with that of L4CBO (Figures S6-S8). For all these crystals, non-bonding 2*p* states of O atoms in occupied states, B-O $\pi$* orbitals and 2*p* states of $BO_3$ substructure in unoccupied states are crucial to the SHG effect. Therefore, the "charge-transfer excitation" from the non-bonding 2*p* states of O atoms to the $\pi$* states and 2*p* states of $BO_3$ (Figure 4b) is the key mechanism of NLO properties for the title crystals. On the contrary, Cs and Rb have a little contribution to SHG in both occupied and unoccupied states.

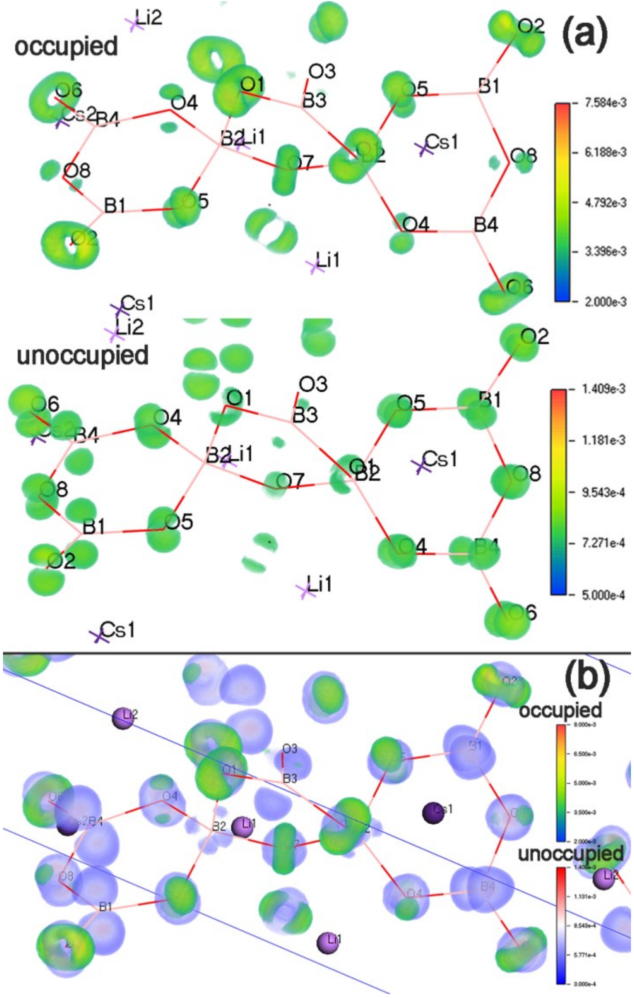

**Figure 4.** (a) The SHG-density of occupied states and unoccupied states. (b) The charge transfer excitation from the nonbonding 2p occupied states of O atoms (green) to the p unoccupied states of B and O (violet) is the key mechanism of NLO properties for L4CBO.

The above analyses clearly show that the BO groups dominate SHG effects in these LMBO series. According to the anionic group theory, the overall SHG coefficients of the crystal is the geometrical superposition of the microscopic second-order susceptibilities of the NLO-active groups. However, a detailed analysis of how the orientation of the NLO-active groups affects the overall NLO effect is still lacking. To further investigate it, the hyperpolarization of isolated BO clusters was calculated using the Hartree-Fock method implemented by the Gaussian09 package[42] at 3-21G level. Figure 5 show the orientations of BO groups in corresponding crystals. The calculated hyperpolarisations of these BO groups with different orientation are listed in Table 3. From it one can see that the antiparallel orientation of $B_5O_{10}$ completely cancel out the three largest tensors and only the smallest $\beta_{14}$ can be constructively superposed, which directly lead to the weak NLO response of L3CBO. As for L4CBO, $B_7O_{14}$ groups have three different orientations with a 120° angel between each other (Figure 5b). Unlike L3CBO, the relative large hyperpolarization tensors, $\beta_{16}$ and $\beta_{22}$, are partly superposed and get a large summation. The $B_{11}O_{22}$ groups are toward the same direction in L6RBO. The biggest tensor is $\beta_{22}$ and all hyperpolarization tensors can be directly superposed.

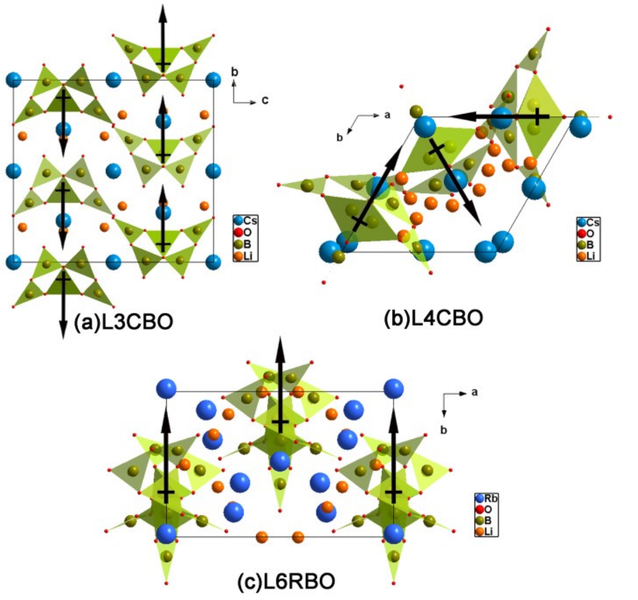

**Figure 5.**The orientations of BO groups in L3CBO, L4CBO and L6RBO. (a) The direction of $B_5O_{10}$ groups pointed in an opposite directions along b axis. (b) Three different kinds of $B_7O_{14}$ groups in L4CBO point along the (100), (010) and ($\bar{1}\,\bar{1}\,0$) directions, respectively. (c) Only one kind of $B_{11}O_{22}$ groups with same direction appears in L6RBO.

| Cluster | Orientation | $\beta_{14}$ | $\beta_{16}$ | $\beta_{22}$ | $\beta_{23}$ | $\beta_{total}$[a] |
|---|---|---|---|---|---|---|
|  | 0° | 2.4 | 43.2 | 9.1 | -44.9 | 7.4 |
| $B_5O_{10}$ | 180° | 2.4 | -43.2 | -9.1 | 44.9 |  |
|  | Sum | 4.8 | 0 | 0 | 0 |  |
|  | 0° | -26.9 | -39.3 | -23.3 | 41.5 | 21.1 |
| $B_7O_{14}$ (L4CBO) | 120° | 13.4 | -15.8 | 47.1 | -20.7 |  |
|  | 240° | 13.4 | -15.8 | 47.1 | -20.8 |  |
|  | Sum | 0 | -71.9 | 71.9 | 0 |  |
|  | 0° | -28.2 | -43.7 | -28.5 | 36.2 | 36.0 |
| $B_7O_{14}$ (L4RBO) | 120° | 14.1 | -16.6 | 52.7 | -18.1 |  |
|  | 240° | 14.1 | -16.6 | 52.7 | -18.1 |  |
|  | Sum | 0 | -76.9 | 76.9 | 0 |  |
| $B_{11}O_{22}$ | 0° | 1.8 | 6.6 | -88.2 | -49.7 | 131.3 |

[a] $\beta_{total} = (\beta_x^2+\beta_y^2+\beta_z^2)^{1/2}$, where $\beta_i = (\beta_{iii}+\beta_{ijj}+\beta_{ikk})$, $i, j, k = x, y, z$

**Table 3.**The calculated hyperpolarization of $B_5O_{10}$, $B_7O_{14}$, and $B_{11}O_{22}$ with different orientation.

## Structure and Properties of the Newly Synthesized $Li_4Rb_3B_7O_{14}$

Through the systematical analyses of the mechanisms of the SHG effects for the three compounds, it was found that the orientation of the BO groups in crystals is one of the key factors to determine the NLO response. The same orientation of $B_{11}O_{22}$ in L6RBO benefits the superposed of the microscopic NLO response. Unfortunately, L6RBO is not phase matchable. As to L3CBO, the antiparallel orientations of $B_5O_{10}$ groups result in a weak NLO response. The arrangement of $B_7O_{14}$ in L4CBO is optimum to obtain a lager superposition of SHG coefficient, and meanwhile, phase matchable in the three crystals. Therefore, L4CBO was chosen as template to obtain a new crystal with better NLO property. The rubidium was chosen to replace caesium to slightly change the substructure of $B_7O_{14}$ but keep the skeleton structure of L4CBO.[43] As we expected, $Li_4Rb_3B_7O_{14}$ (L4RBO) with a larger SHG response than L4CBO was obtained through solid state reaction.

The newly synthesized L4RBO is isomorphic with L4CBO, and belongs to the space group $P3_121$ (No.152). Relevant crystallographic data are listed in Table 4. The 3D network was built from isolated $B_7O_{14}$ units interconnected by $LiO_n$ (n= 4, 5) and distorted polyhedral $RbO_{10}$ (Figure 6). The primary building units in L4RBO are $B_7O_{14}$ consisting of three six-member ring motif in which two $B_3O_7$ rings are connected by a $B_3O_8$ ring. The triangularly coordinated boron atoms have B-O distances in the range 1.315(4)-1.435(4) Å [av = 1.372 Å], and the tetrahedral B atoms have longer B-O distances in the range of 1.450(4)-1.489(3) Å [av = 1.466 Å]. $Li(1)O_4$ and $Li(2)O_5$ polyhedra are interconnected via sharing their vertexes and edges into a 3D framework with Li-O bond distances ranging from 1.806 to 2.370 Å and an average bond distance of 2.0459 Å. $Rb(1)O_{10}$ and $Rb(2)O_{10}$ polyhedra are interconnected by shared oxygen atoms to form the 3D framework with Rb–O bond distances ranging from 2.830(3) to 3.555(4) Å and an average bond distances of 3.2333 Å (Figure S10). Compared with the average bond length of Cs-O of 3.3323 Å, the Rb-O bond distance is shorter, and consequently results in a decrease of unit cell dimensions for L4RBO.

| Empirical formula | $Li_4Rb_3B_7O_{14}$ |
|---|---|
| Formula weight | 583.84 |
| Temperature | 153(2) K |
| Wavelength | 0.71073 Å |
| Crystal system | trigonal |
| space group | $P3_121$ |
| Unit cell dimensions | a = 6.8765(5) Å<br>c = 25.923(4) Å |
| Volume | 1061.56(19) $Å^3$ |
| Calculated density | 2.740 $g/cm^3$ |
| Z | 3 |
| Absorption coefficient | 10.403 $mm^{-1}$ |
| F(000) | 810 |
| Crystal size | 0.11× 0.19 × 0.20 mm |
| Theta range for data collection | 2.36 to 27.46 deg. |
| Limiting indices | $-8\le h\le 5$, $-7\le k\le 8$, $-33\le l\le 33$ |
| Reflections collected / unique | 6472 / 1618 [R(int) = 0.0321] |
| Completeness to theta = 27.46 | 100.0 % |
| Max. and min. transmission | 0.3623 and 0.5853 |
| Refinement method | Full-matrix least-squares on $F^2$ |
| Data / restraints / parameters | 1618 / 0 / 129 |
| Goodness-of-fit on $F^2$ | 1. 042 |
| Final R indices [I>2sigma(I)] [a] | $R_1 = 0.0202$, $wR_2 = 0.0434$ |
| R indices (all data) [a] | $R_1 = 0.0234$, $wR_2 = 0.0442$ |
| Extinction coefficient | 0.005(9) |
| Largest diff. peak and hole | 0.334 and -0.524 $eÅ^3$ |

[a] $R_1 = \Sigma||F_o| - |F_c||/\Sigma|F_o|$ and $wR_2 = [\Sigma w(F_o^2 - F_c^2)^2 / \Sigma w F_o^4]^{1/2}$ for $F_o^2 > 2\sigma(F_o^2)$

**Table 4.** Crystal data and structure refinement for $Li_4Rb_3B_7O_{14}$.

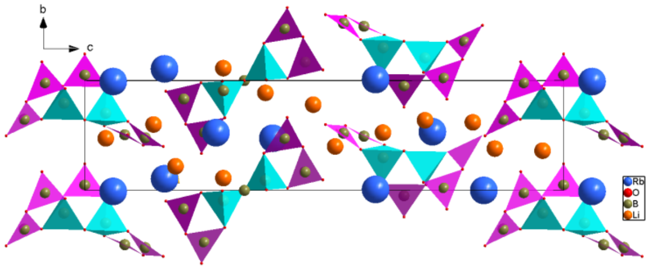

**Figure 6.** View of the structure of $Li_4Rb_3B_7O_{14}$ down the *a* axis.

The infrared (IR) spectroscopy of L4RBO reveals the different stretching type of trigonal $BO_3$ and tetrahedral $BO_4$ (Figure S11).[44, 45] The similar IR spectrum shapes of L4RBO and L4CBO further testify that the two crystals are isomorphic and share same BO groups. As shown in Figure S12, there are two endothermic peaks on the DSC curve, along with weight loss on the TGA curve upon melting. It illustrates that L4RBO melt incongruently. In order to further verify that, 0.5 g of L4RBO powder was packed into a platinum crucible, heated to 900 °C, and then rapidly cooled to room temperature. Analysis of the powder XRD pattern of the solidified melt revealed that the entire solid product exhibited a diffraction pattern different from that of the initial L4RBO powder (see Figure S13). This doubtlessly demonstrates that L4RBO is an incongruently melting compound. Therefore, the flux method is necessary for the purpose of its crystal growth.

The UV-Vis-NIR diffuse reflectance spectrum of L4RBO converted by the KM transformation is shown in Figure S2, the spectrum shows a smaller experimental optical gap of 5.51 eV than that of 6.01 eV for L4CBO. The SHG measurements on the sieved L4RBO sample indicate that it is phase matchable (Figure 7) with a SHG efficiency about 2/3 of the value of KDP. The calculated $d_{11}$ is 0.335 pm/V, which is well in agreement with the experimental one (Table 2). Both the experimental and calculated results show that L4RBO exhibit a higher SHG efficiency than that of L4CBO. One may speculate that the lower band gap of L4RBO is reflected in the high SHG efficiency. However, when a scissors operator is used to increase the band gap of L4RBO be equal to that of L4CBO, the calculated $d_{11}$ is 0.283 pm/V, which is still larger than that of L4CBO. It implies that the structural change of BO groups is also a reason that results in an increase of SHG coefficients in L4RBO. The bigger dipole moment of $B_7O_{14}$ cluster in L4RBO show a greater distortion compared with that in L4CBO (see Figure S13). Additionally, the calculated hyperpolarization of $B_7O_{14}$ cluster in L4RBO is also bigger than the counterpart in L4CBO (Table 2). It means that, in addition to a lower band gap, the structural changes of $B_7O_{14}$, derived from replacement of cations, result in a higher SHG efficiency in L4RBO. The electronic structure, the band-resolved $\chi^{(2)}$ results, and SHG density of L4RBO are listed with those of the previous LMBOs. All of these results confirm the conclusion that drawn from L3CBO, L4CBO, and L6RBO.

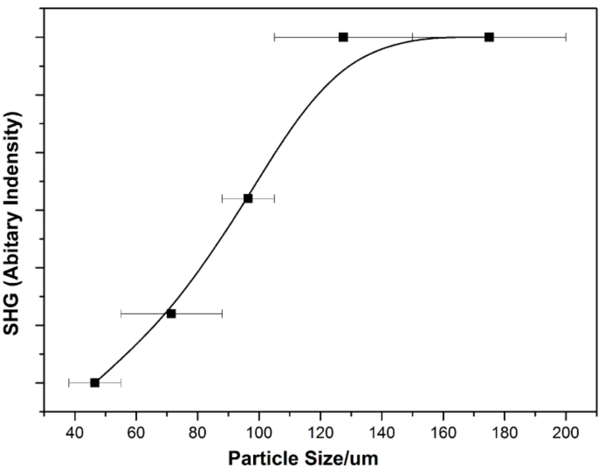

**Figure 7.** The Phase-matching, that is, particle size vs SHG intensity, data for L4RBO. The solid curve drawn is to guide the eye and is not a fit to the data.

## Conclusions

In summary, the properties of synthesized $Li_nM_{n-1}B_{2n-1}O_{4n-2}$ (M=Cs/Rb, n=3, 4, 6) are further analyzed, they have the topologically similar BO structure. The electronic structure calculations show L3CBO, L4CBO, and L6RBO are all indirect gap materials. Their band structures and PDOS are similar to one another due to their similar composition and BO topological structure. The similarity of the isolated BO groups in the title compounds guides us to explore its role in SHG effect. Through the band-resolved method and SHG-density method, the dominant orbitals and NLO-active units giving major contributions to the $\chi^{(2)}$ tensors for each crystal are identified and further analyzed. On the basis of these calculations, several useful conclusions are extracted. The non-bonding 2*p* states of O atoms in occupied states and *π** and 2*p* states of $BO_3$ substructure in unoccupied states are crucial to SHG effect. On the contrary, Cs and Rb have a little contribution in both occupied and unoccupied states. Furthermore, the apparent differences in the collective alignment of BO groups in these LMBO series suggest a global mechanism of the origin of SHG effects should be explored. The hyperpolarization of isolated BO clusters in the corresponding crystals was calculated to investigate how the orientation of the NLO-active groups affects the overall NLO effect. The results show that the orientation of the BO groups in the title crystals is one of the key factors to determine the NLO response.

Through the systematical analyses of the mechanisms of the SHG effects for the three compounds, we find that the collective alignment of $B_7O_{14}$ in L4CBO is the optimum arrangement to obtain a lager superposition of SHG coefficient and phase matchable in the three crystals. Therefore, a new crystal L4RBO was designed by choosing L4CBO as template, and the rubidium atom was chosen to replace caesium to change the substructure of $B_7O_{14}$ but keep the skeleton structure of L4CBO. As we expected, L4RBO with a short UV cutoff edge (below 190 nm) and a larger SHG response than L4CBO was obtained through solid state reaction. The electronic structure, SHG coefficients, the band-resolved results as well as SHG density of newly synthesized L4RBO confirm the conclusion drawn from L3CBO, L4CBO, and L6RBO.

## Acknowledgements

This work is supported by National Basic Research Program of China (Grant No. 2014CB648400), the "National Natural Science Foundation of China" (Grant Nos. U1129301, and U1303193), Ming-Hsien Lee thanks NCHC for database responses support and Key Win Electronics Co. for equipment donation.

## Notes and references

[a] Key Laboratory of Functional Materials and Devices for Special Environments of CAS; Xinjiang Key Laboratory of Electronic Information Materials and Devices; Xinjiang Technical Institute of Physics & Chemistry of CAS, 40-1 South Beijing Road, Urumqi 830011, China.
[b] University of Chinese Academy of Sciences, Beijing 100049, China;
[c] Department of Physics, Tamkang University, Taipei 25137, Taiwan
To whom correspondence should be addressed.
E-mail: zhyang@ms.xjb.ac.cn (Zhihua Yang), slpan@ms.xjb.ac.cn (Shilie Pan), yangyun@ ms.xjb.ac.cn (Yun Yang)
Tel: (86)-991-3810816
Fax: (86)-991-3838957

†Electronic Supplementary Information (ESI) available: Calculation results of the other crystals in the LMBO series, experimental result and crystallographic data of new sythesized $Li_4Rb_3B_7O_{14}$. See DOI: 10.1039/b000000x/

1. C. Chen, T. Sasaki, R. Li, Y. Wu, Z. Lin, Y. Mori, Z. Hu, J. Wang, S. Uda, M. Yoshimura and Y. Kaneda, in *Nonlinear Optical Borate Crystals*, Wiley-VCH Verlag & Co. KGaA, 2012, ch. 1, pp. 1-11.
2. H. Huang, J. Yao, Z. Lin, X. Wang, R. He, W. Yao, N. Zhai and C. Chen, *Angew. Chem. Int. Ed.*, 2011, 50, 9141-9144.
3. H. Wu, H. Yu, Z. Yang, X. Hou, X. Su, S. Pan, K. R. Poeppelmeier and J. M. Rondinelli, *J. Am. Chem. Soc.*, 2013, 135, 4215-4218.
4. M. Xia and R. Li, *J. Solid State Chem.*, 2013, 201, 288-292.
5. M. Xia and R. Li, *J. Solid State Chem.*, 2013, 197, 366-369.
6. S. Zhao, G. Zhang, J. Yao and Y. Wu, *Mater. Res. Bull.*, 2012, 47, 3810-3813.
7. C. Chen, B. Wu, A. Jiang and G. You, *Sci. Sin. Ser. B*, 1985, 28, 235-243.
8. C. Chen, Y. Wu, A. Jiang, B. Wu, G. You, R. Li and S. Lin, *J. Opt. Soc. Am. B*, 1989, 6, 616-621.
9. Y. Wu, T. Sasaki, S. Nakai, A. Yokotani, H. Tang and C. Chen, *Appl. Phys. Lett.*, 1993, 62, 2614-2615.
10. J.-M. Tu and D. A. Keszler, *Mater. Res. Bull.*, 1995, 30, 209-215.
11. C. Chen, N. Ye, J. Lin, J. Jiang, W. Zeng and B. Wu, *Adv. Mater.*, 1999, 11, 1071-1078.
12. T. Sasaki, Y. Mori and M. Yoshimura, *Opt. Mater.*, 2003, 23, 343-351.
13. Z. Lin, J. Lin, Z. Wang, C. Chen and M.-H. Lee, *Phys. Rev. B*, 2000, 62, 1757-1764.
14. C. Chen, in *Materials for Nonlinear Optics*, American Chemical Society, 1991, vol. 455, ch. 24, pp. 360-379.
15. P. Becker, *Adv. Mater.*, 1998, 10, 979-992.

16. M.-H. Lee, C.-H. Yang and J.-H. Jan, *Phys. Rev. B*, 2004, 70, 235110-235120.
17. C.-h. Lo, *Master Degree Thesis, Tamkang University*, 2005.
18. Y. Yang, S. Pan, J. Han, X. Hou, Z. Zhou, W. Zhao, Z. Chen and M. Zhang, *Cryst. Growth Des.*, 2011, 11, 3912-3916.
19. Y. Yang, S. Pan, X. Hou, C. Wang, K. R. Poeppelmeier, Z. Chen, H. Wu and Z. Zhou, *J. Mater. Chem.*, 2011, 21, 2890-2894.
20. Y. Yang, S. Pan, H. Li, J. Han, Z. Chen, W. Zhao and Z. Zhou, *Inorg. Chem.*, 2011, 50, 2415-2419.
21. S. J. Clark, M. D. Segall, C. J. Pickard, P. J. Hasnip, M. J. Probert, K. Rrfson and M. C. Payne, *Z. Kristallogr*, 2005, 220, 567-570.
22. M.-H. Lee, *Ph.D. Thesis,The University of Cambridge*, 1996.
23. J. Lin, A. Qteish, M. Payne and V. Heine, *Phys. Rev. B*, 1993, 47, 4174-4180.
24. A. M. Rappe, K. M. Rabe, E. Kaxiras and J. D. Joannopoulos, *Phys. Rev. B*, 1990, 41, 1227-1230.
25. J. P. Perdew, K. Burke and M. Ernzerhof, *Phys. Rev. Lett.*, 1996, 77, 3865-3868.
26. C. Aversa and J. E. Sipe, *Phys. Rev. B*, 1995, 52, 14636-14645.
27. J. Lin, M. H. Lee, Z. P. Liu, C. T. Chen and C. J. Pickard, *Phys. Rev. B*, 1999, 60, 13380-13389.
28. SAINT, version 7.60A (2008) Bruker Analytical X-ray Instruments, Inc Madison, WI.
29. S. Sheldrick GM, Version 6.14 (2003) Bruker Analytical X-ray Instruments. Inc Madison, WI.
30. A. L. Spek, *J. Appl. Crystallogr.*, 2003, 36, 7-13.
31. P. Kubelka and F. Munk, *Z. Tech. Phys.*, 1931, 12, 593-601.
32. J. Tauc, *Mater. Res. Bull.*, 1970, 5, 721-729.
33. X. Y. Fan, S. L. Pan, X. L. Hou, X. L. Tian, J. Han, J. Haag and K. R. Poeppelmeier, *Cryst. Growth Des.*, 2010, 10, 252-256.
34. G. Yuan and D. Xue, *Acta Crystallogr. B*, 2007, 63, 353-362.
35. O. Schevciw and W. B. White, *Mater. Res. Bull.*, 1983, 18, 1059-1068.
36. R. French, J. Ling, F. Ohuchi and C. Chen, *Phys. Rev. B*, 1991, 44, 8496-8502.
37. J. Lin, M.-H. Lee, Z.-P. Liu, C. Chen and C. J. Pickard, *Phys. Rev. B*, 1999, 60, 13380-13389.
38. Y. Liu, L. Wei, F. Yu, Z. Wang, Y. Zhao, S. Han, X. Zhao and X. Xu, *CrystEngComm*, 2013, 15, 6035-6039.
39. A. D. Becke, *J. Chem. Phys.*, 1993, 98, 5648-5652.
40. Z. Lin, Z. Wang, C. Chen, S. K. Chen and M.-H. Lee, *J. Appl. Phys.*, 2003, **93**, 9717-9723.
41. C.-g. Duan, J. Li, Z.-q. Gu and D.-s. Wang, *Phys. Rev. B*, 1999, 60, 9435-9443.
42. M. J. Frisch, G. W. Trucks, H. B. Schlegel, G. E. Scuseria, J. R. C. M. A. Robb, G. Scalmani, V. Barone, B. Mennucci, G. A. Petersson, H. Nakatsuji, M. Caricato, X. Li, H. P. Hratchian, A. F. Izmaylov, J. Bloino, G. Zheng, J. L. Sonnenberg, M. Hada, M. Ehara, K. Toyota, R. Fukuda, J. Hasegawa, M. Ishida, T. Nakajima, Y. Honda, O. Kitao, H. Nakai, T. Vreven, J. J. A. Montgomery, J. E. Peralta, F. Ogliaro, M.Bearpark, J. J. Heyd, E. Brothers, K. N. Kudin, V. N. Staroverov, R. Kobayashi, K. R. J. Normand, A. Rendell, J. C. Burant, S. S. Iyengar, J. Tomasi, M. Cossi, N. Rega, J. M. Millam, M. Klene, J. E. Knox, J. B. Cross, V. Bakken, C. Adamo, J. Jaramillo, R. Gomperts, R. E. Stratmann, O. Yazyev, A. J. Austin, R. Cammi, C. Pomelli, J. W. Ochterski, R. L. Martin, K. Morokuma, V. G. Zakrzewski, G. A. Voth, P. Salvador, J. J. Dannenberg, S. Dapprich, A. D. Daniels, Ö. Farkas, J. B. Foresman, J. V. Ortiz, J. Cioslowski and G. D. J. Fox, Inc., Wallingford CT, 2009. , *Gaussian 09, Revision C.01*.
43. R. E. Sykora, K. M. Ok, P. S. Halasyamani and T. E. Albrecht-Schmitt, *J. Am. Chem. Soc.*, 2002, 124, 1951-1957.
44. L. Jun, X. Shuping and G. Shiyang, *Spectrochim. Acta A*, 1995, 51, 519-532.
45. Z. Liu, S. Li and C. Zuo, *Thermochim. Acta*, 2005, 433, 196-199.